Research article

# Validation of a SIMIND Monte Carlo modelled gamma camera for Iodine-123 and Iodine-131 imaging

Michaella Morphis [a,*], Johan A. van Staden [a], Hanlie du Raan [a], Michael Ljungberg [b]

[a] Department of Medical Physics, Faculty of Health Sciences, University of the Free State, Bloemfontein, South Africa
[b] Medical Radiation Physics, Lund University, Lund, Sweden

ARTICLE INFO

ABSTRACT

*Purpose:* Monte Carlo (MC) modelling techniques can assess the quantitative accuracy of both planar and SPECT Nuclear Medicine images. It is essential to validate the MC code's capabilities in modelling a specific clinical gamma camera, for radionuclides of interest, before its use as a clinical image simulator. This study aimed to determine if the SIMIND MC code accurately simulates emission images measured with a Siemens Symbia™ T16 SPECT/CT system for I-123 with a LEHR and a ME collimator and for I-131 with a HE collimator.
*Methods:* The static and WB planar validation tests included extrinsic system energy pulse-height distributions (EPHDs), system sensitivity and system spatial resolution in air as well as a scatter medium. The SPECT validation test comprised the sensitivity from a simple geometry of a sphere in a cylindrical water-filled phantom.
*Results:* The system EPHDs compared well, with differences between measured and simulated primary photopeak FWHM values not exceeding 4.6 keV. Measured and simulated planar system sensitivity values displayed percentage differences less than 6.9% and 6.3% for static and WB planar images, respectively. Measured and simulated planar system spatial resolution values in air showed percentage differences not exceeding 6.4% (FWHM) and 10.0% (FWTM), and 5.1% (FWHM) and 5.4% (FWTM) for static and WB planar images, respectively. For static planar system spatial resolution measured and simulated in a scatter medium, percentage differences of FWHM and FWTM values were less than 5.8% and 12.6%, respectively. The maximum percentage difference between the measured and simulated SPECT validation results was 3.6%.
*Conclusion:* The measured and simulated validation results compared well for all isotope-collimator combinations and showed that the SIMIND MC code could be used to accurately simulate static and WB planar and SPECT projection images of the Siemens Symbia™ T16 SPECT/CT for both I-123 and I-131 with their respective collimators.

## 1. Introduction

Due to the increased interest in theranostics in Nuclear Medicine (NM), the importance of image quantification using iodine-131 (I-131) and iodine-123 (I-123) has been re-emphasised (Silberstein 2012; Sjögreen et al., 2002; Yordanova et al., 2017). I-131 is one of the earliest radionuclides used for radionuclide therapy. Since the 1940s, I-131 has been used to treat differentiated thyroid carcinoma, and is the radionuclide of choice for thyroid diseases (Thomas 2002). However, it has gained popularity in the treatment of non-Hodgkin lymphomas and neuroendocrine tumours (NETs). I-131 emits a principal gamma photon of 364.5 keV (81.2% abundance), one with 284.3 keV (6.1% abundance) and two higher energy photons of 636.9 keV (7.1% abundance) and 722.9 keV (1.8%

abundance). Despite the low abundance of these two high-energy photons, they are still of importance due to their ability to penetrate the gamma cameras' collimator septa. I-131 has a physical half-life of 8.04 days and also emits beta particles with a maximum and mean energy of 606.0 keV and 192.0 keV, respectively (Kellett et al., 2017). Iodine naturally accumulates in the thyroid; however, it can be attached to a pharmaceutical, allowing targeted imaging and therapy. I-131 labelled to a noradrenaline analogue, meta-iodobenzylguanidine (MIBG), is typically used to detect and treat NETs. It naturally accumulates in NETs as well as the lungs, liver, kidneys, spleen, bladder, bone marrow and salivary glands (Bombardieri et al., 2010; Giammarile et al., 2008).

In contrast to I-131, which emits both gamma photons and beta particles, I-123 is a pure gamma photon emitter. It emits a principal

* Corresponding author.
  *E-mail address:* michaellamorphis@icloud.com (M. Morphis).

gamma photon of 159.0 keV (83.2% abundance) and additionally at 27.3 keV (70.7% abundance) and 528.9 keV (1.3% abundance) and has a physical half-life of 13.2 h. These characteristics make I-123 ideal for diagnostic imaging. Since the uptake pattern of I-123 and I-131 are similarly in the body, I-123 can be used in a treatment planning process of I-131 radionuclide therapy. I-123 carries a reduced radiation burden compared to I-131 due to its shorter half-life and lack of beta particles, and higher quantities of I-123 can therefore be administered for diagnostic purposes. As with I-131-MIBG, I-123-MIBG naturally accumulates in NETs as well as the lungs, liver, kidneys, spleen, bladder, bone marrow and salivary glands.

Because of the accumulation of these radiopharmaceuticals in healthy normal tissue, accurate dose calculations should be performed prior to therapy to predict the radiation burden organs at risk may encounter. The accuracy of absorbed dose calculations depends on several factors such as tumour and organ size, but most importantly on the radiopharmaceuticals' biokinetics. Factors that influence the estimation of biokinetic data include, but are not limited to, image modality and the collimator-isotope combination used. Biokinetic information can be estimated from static or whole-body (WB) planar 2D images, or single photon emission computed tomography (SPECT) 3D images. The use of quantitative SPECT imaging at multiple time points is potentially quantitatively more accurate in comparison to those obtained from planar imaging, considering it is a 3D modality. However, SPECT imaging can be highly time-consuming due to longer acquisition times and the limited field of view which required more than one bed-position acquisition. A compromise is to use the hybrid WB planar/SPECT dosimetry method, proposed by Ljungberg and Gleisner (2015). This method uses a set of WB data at multiple time points, to obtain the shape of the time-activity curve for a specific organ, which is then scaled to a single SPECT quantitative data point obtained at a single time point. This method can be useful in the case of large patient throughputs, since results in dosimetry accuracies are comparable to that of multiple SPECT/CT images but with the speed of planar imaging (Garkavij et al., 2010).

The isotope-collimator combination is another important factor to consider. Imaging I-131 with a high energy (HE) collimator is well established (Dewaraja et al., 2013), but it is not clear as to whether I-123 imaging should be performed with a low energy high resolution (LEHR) collimator or a medium energy (ME) collimator. For quantitatively accurate images, the ME collimator's use is favoured, as it reduces the effect of collimator septal scatter and penetration, resulting in improved image contrast (Rault et al., 2007). However, the LEHR collimator can provide superior spatial resolution images, but only if appropriate scatter and collimator resolution corrections are applied (Dobbeleir et al., 1999; Rault et al., 2007).

Monte Carlo (MC) techniques have played a significant role in the NM discipline and have become a method of choice to optimise instrumentation and clinical protocols, enhance image correction techniques, and develop and implement patient-specific dosimetry (Ljungberg et al., 2012). By MC simulations, researchers can investigate what influence a parameter has on a system's performance and study the effect that a parameter has, in a way that otherwise is difficult or even impossible to measure (Zaidi 1999). The MC method has been applied extensively in the modelling of gamma cameras for radionuclides, including technetium-99m, I-131 and lutetium-177 (Bahreyni Toossi et al., 2010; Dewaraja et al., 2013; Ljungberg et al., 2016). There are various MC simulation codes available for NM imaging, such as SIMIND, SimSET and GATE (Ljungberg et al., 1998; Zaidi, 1999; Jan et al., 2011; Sarrut et al., 2014).

In this study, we have used the SIMIND MC code which models a standard clinical scintillation camera for both planar and SPECT acquisitions (Ljungberg and Strand 1989). SIMIND has been extensively used to estimate the quantification accuracy of planar and SPECT imaging (Kalantari et al., 2012; Minarik et al., 2008; Zaidi 1999). The energy resolution (ER) was simulated based on a fitted model

($ER = a + b\sqrt{Energy + (c \times Energy^2)}$) where $a$, $b$ and $c$ are estimated from measured data), as described by Morphis et al. (2021). This ER estimation method was used in this study since recent results reported a significant improvement in the modelling of ER of high-energy photon emitting radionuclides (e.g., I-131), as well as for radionuclides with multiple photopeaks (e.g., I-131, I-123 and lutetium-177).

It is essential to validate any MC codes' capability in modelling a specific clinical gamma camera for the radionuclides of interest prior to its use as a clinical simulator (Staelens et al., 2003). The SIMIND program has been used to model gamma cameras for radionuclides, including technetium-99m, I-131 and lutetium-177 (Bahreyni Toossi et al., 2010; Ejeh et al., 2018; Islamian et al., 2012; Ramonaheng et al., 2020). However, to our knowledge, modelling of the Siemens Symbia™ T16 gamma camera with SIMIND using a fitted ER model for I-123 with both the LEHR and ME collimators and I-131 with the HE collimator has not been reported.

This study therefore aimed to validate the SIMIND modelling of a Siemens Symbia™ T16 SPECT/CT system for I-123 using the LEHR and ME collimators (referred to as I-123 LEHR and I-123 ME, respectively) and I-131 using the HE collimator (referred to as I-131 HE), by comparing gamma camera measurements with simulations. A successful validation can further facilitate a more extensive evaluation of static planar, WB planar and SPECT I-123 and I-131 activity quantification accuracy using simulations.

A WB planar scan measurement differs in its principles from a static planar measurement in that it involves a continuous bed motion in an axial direction, with a pre-set scanning speed. Since motion of the bed during an ongoing acquisition may influence image quality the performance criterion for WB planar imaging was therefore validated in addition to static planar imaging.

## 2. Materials and methods

The dual-head Siemens Symbia™ T16 (Siemens Healthcare, Erlangen, Germany) SPECT gamma camera is a SPECT/CT system used at Universitas Academic Hospital (Bloemfontein, South Africa). A series of static planar, WB planar and SPECT tests were measured on the gamma camera. These tests were then simulated using version 6.2 of the SIMIND MC code. Where applicable, the percentage difference and the difference between measured and simulated values were reported.

$$\% \; Difference = \frac{simulated \; value - measured \; value}{measured \; value} \times 100 \qquad (1)$$

$$Difference = simulated \; value - measured \; value \qquad (2)$$

The planar validation tests included a comparison of measured and simulated extrinsic (with a collimator); energy pulse-height distributions (EPHDs), static and WB planar system sensitivity and system spatial resolution in air (in-air spatial resolution). Additionally, the static planar system spatial resolution was obtained in a scattering medium (in-scatter spatial resolution). These specific tests were chosen in accordance with literature reports for MC gamma camera validations (Bahreyni Toossi et al., 2010; Ejeh 2019; Ramonaheng et al., 2020).

The SPECT validation test compared the measured and simulated SPECT sensitivity values obtained using the simple geometry of a sphere of activity in a cylindrical water-filled phantom.

All measurements and simulations were performed for (i) I-123 LEHR, (iii) I-123 ME, and (iii) I-131 HE. Photopeak data was obtained within a 15% energy window centred over the 159.0 keV and 364.5 keV photopeaks for I-123 and I-131, respectively.

### 2.1. Measurements

All static and WB planar measurements were acquired with a single detector only, as the gamma camera acceptance tests showed little

difference between the system's two detectors. The amount of radioactivity used was sufficiently low that the camera did not display any dead-time effects; thus, no dead-time correction was necessary. Before measurements, the detector was peaked relative to the 159.0 keV and 364.5 keV photopeak's for all I-123 and I-131 measurements, respectively. SPECT measurements were, however, conducted using both detectors to increase sensitivity for a given acquisition time.

I-123 and I-131 activities were measured using a Biodex Atomlab 500 dose calibrator (Biodex Medical Systems, New York, NY, USA). The accuracy of the dose calibrator for both I-123 and I-131 was traceable to a secondary standard through the National Institute of South Africa (NMISA) in Cape Town, South Africa.

CT images were acquired for each static planar, WB planar and SPECT validation test setup, for use in both the SIMIND simulation and in the reconstruction processes, as explained below. The CT images were acquired in a standard imaging protocol (image matrix: $512 \times 512$, pixel size: $1.2 \times 1.2$ mm$^2$, slice thickness: 5.0 mm, reconstruction kernel: standard smoothing body kernel (B08s)).

### 2.1.1. Static planar validation tests

The validation procedure for static planar imaging was performed according to guidelines stipulated in the National Electrical Manufacturers Association (NEMA) recommendations for gamma camera performance criteria (National Electrical Manufacturers Association 2012).

*2.1.1.1. Energy pulse-height distributions.* Extrinsic EPHDs (spectrum showing the distribution of counts as a function of photon energy, acquired with a collimator) were acquired from small point-like I-123 and I-131 sources, positioned on a Styrofoam block at source-to-collimator distances (SCDs) of $150 \pm 2$ mm, $300 \pm 2$ mm, and $650 \pm 2$ mm (Figure 1a). The EPHDs were acquired from the respective sources in air to obtain 30 000 counts in the channel with the highest count contribution. The acquired EPHDs were exported from the manufacturer's computer and analysed using the public domain software, ImageJ

(version 1.52r) (Ferreira and Rasband 2012). Each energy pulse-height distribution (EPHD) was corrected for background radiation. A Gaussian function was fitted to the main emission photopeak data points, and the full width at half maximum (FWHM) values were calculated and reported in keV for each photopeak.

*2.1.1.2. System sensitivity.* A petri-dish (internal diameter: 87 mm) was filled with a homogenous solution of 92.8 MBq of I-123, up to a depth of $\pm 2$ mm. The petri-dish was positioned on a Styrofoam block in the centre of the detector's field-of-view, at a source-to-collimator distance (SCD) of $100 \pm 2$ mm (Figure 1b). A four-million-count static planar image was acquired in a $256 \times 256$ image matrix with a pixel size of $2.4 \times 2.4$ mm$^2$. A second petri-dish of 61.8 MBq of I-131 was filled in the same way, and the acquisition was repeated. The count rate in counts per second (cps) in a region-of-interest (ROI) with dimensions equal to that of the detector's useful-field-of-view (UFOV) was calculated. The system sensitivity, for each isotope-collimator combination, was calculated as follows,

$$Sensitivity\ (cps\ /\ MBq) = \frac{count\ rate\ (cps)}{decay\ corrected\ activity\,(MBq)} \qquad (3)$$

*2.1.1.3. In-air spatial resolution.* A pair of capillary tubes was filled with 24.0 MBq of I-123 each and placed on a Styrofoam block, $100 \pm 2$ mm apart, at SCDs of $50 \pm 2$ mm, $100 \pm 2$ mm, and $150 \pm 2$ mm (Figure 1c). Static planar images were acquired in a $512 \times 512$ image matrix with a pixel size of $1.2 \times 1.2$ mm$^2$ until at least 10 000 counts in the peak location of each line spread function (LSF) was reached. An additional pair of capillary tubes was filled with 24.0 MBq of I-131 each, and static planar images were acquired, as before, at the same three distances. Profiles representing line-spread functions (LSFs) for each capillary tube were obtained from the measured images. Each LSF profile was fit with a Gaussian function, and from this fit, the FWHM and full width at tenth maximum (FWTM) values were calculated and reported in mm.
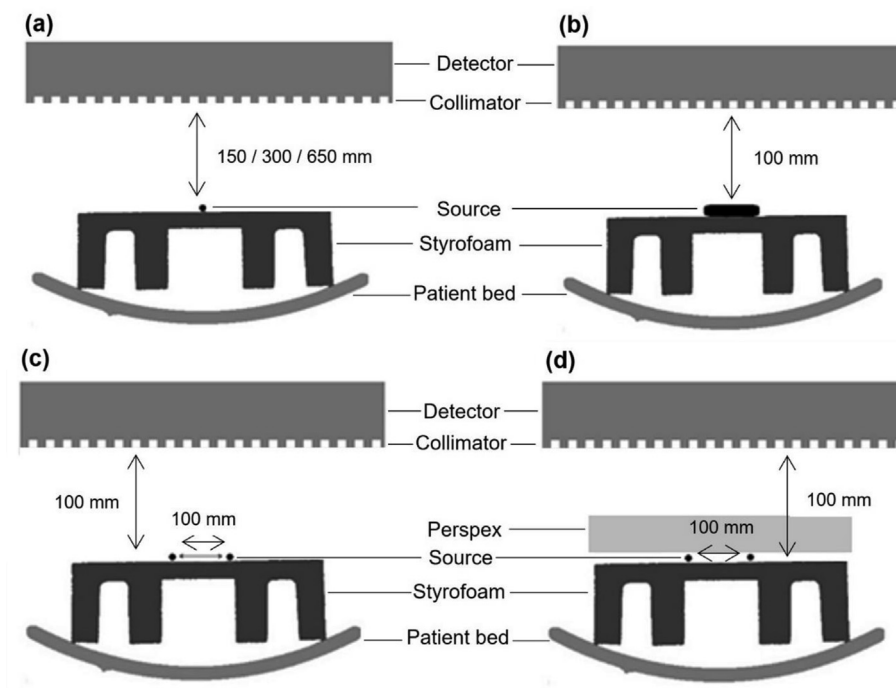


**Figure 1.** Gamma camera setup for the acquisition of (a) EPHD, (b) system sensitivity, (c) system in-air spatial resolution and (d) system in-scatter spatial resolution.

*2.1.1.4. In-scatter spatial resolution.* Planar static images were acquired, as above, but differed in that a 50 mm slab of Perspex® was positioned on top of the capillary tubes to introduce scatter (Figure 1d). FWHM and FWTM values were calculated for all isotope-collimator combinations.

### 2.1.2. Whole-body planar validation tests

In this study, all WB planar images were acquired with the standard clinical imaging protocol (scan speed: 6.0 cm/min, image matrix size: $256 \times 1024$, pixel size: $2.4 \times 2.4$ mm$^2$). The sources were positioned at a SCD of $100 \pm 2$ mm.

*2.1.2.1. System sensitivity.* Using the setup, as shown in Figure 1a, WB planar system sensitivity images were acquired for all three isotope-collimator combinations. Similar to the static planar sensitivity, the WB system sensitivity was calculated using Eq. (3) and counts obtained in a ROI, with dimensions equal to that of the detectors' useful field of view.

*2.1.2.2. In-air spatial resolution.* WB planar system spatial resolution images were acquired in both the X and Y orientations, using the setup, as shown in Figure 1b, for the three isotope-collimator combinations. Average FWHM and FWTM values were obtained and reported, as described for the static planar spatial resolution images.

### 2.1.3. SPECT validation test

A SPECT sensitivity value was obtained from a simple geometry of a sphere suspended in a water-filled cylindrical phantom (diameter: 216 mm, height: 186 mm), as shown in Figure 2. Two spheres (diameter: 42 mm) were filled with 164.1 MBq and 86.9 MBq of I-123 and I-131, respectively. SPECT projection images were acquired using the standard clinical imaging protocol (step and shoot mode, non-circular orbit of rotation, 60 projections, 40 s per projection, matrix size: $128 \times 128$, pixel size: $4.8 \times 4.8$ mm$^2$). Images were acquired for all isotope-collimator combinations.

The SPECT projection images were reconstructed using an ordered subset expectation maximisation (OSEM) iterative reconstruction package, developed by Frey and Tsui (1996), which is incorporated into a software developed at Lund University, Sweden (Sjögreen et al., 2005). The iterative reconstruction performs a CT-based attenuation correction, model-based scatter correction by the Effective Scatter Source Estimation (ESSE), and a collimator response correction, which includes septal penetration and scatter corrections, using precalculated MC simulated kernels. In this study, the SPECT images were reconstructed with six iterations and six subsets, into a $128 \times 128 \times 128$ matrix with a voxel size of $4.8 \times 4.8 \times 4.8$ mm$^3$.

Using the public domain software Amide (Loening and Gambhir 2001), spherical VOIs, corresponding to each sphere's physical size, were used to obtain the sphere counts (using fractional voxels which is the sum of voxel weights giving an indication of how large a region is in voxel space, instead of total voxels which is the total number of voxels both partial and total inclusion). Results were reported in units of cps/MBq for all three isotope-collimator combinations.
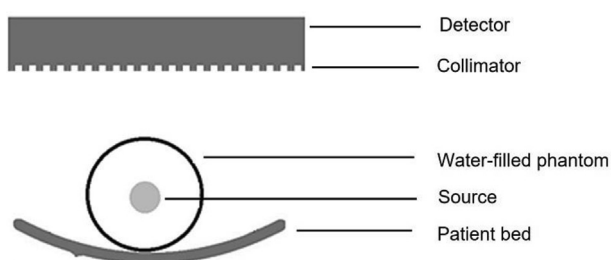


**Figure 2.** Gamma camera setup for the SPECT acquisition of sphere in a water-filled cylindrical phantom.

### 2.2. Simulations

The above-mentioned static planar, WB planar and SPECT validation test measurements were simulated using the SIMIND code. Voxel-based digital phantoms were created from the CT images obtained for each measurement setup to ensure the simulation setup was comparable. This process, together with the gamma camera's physical parameters (including intrinsic characteristics) and setup (including backscatter elements), as used in this study, has recently been described by Morphis et al. (2021). It is important to note that the collimators were modelled with particle tracking, allowing for collimator septal scatter and penetration modelling.

The variation of the ER was modelled by a fitted ER function, ($ER = a + b\sqrt{Energy + (c \times Energy^2)}$), proposed by Morphis et al. (2021). The fitted model is estimated from measured data and was found to better model the gamma cameras' ER over the complete energy range when compared to the $1/\sqrt{Energy}$ model that varies with an energy-dependent ER relative to a known value for a reference energy, as described in Cherry et al. (2003).

Acquisition parameters (image matrix size, pixel size, energy window settings, activity values, acquisition time and isotope-collimator combinations) were kept the same as that used during the measurements, as described in Section 2.1.

### 2.2.1. Static planar validation tests

Static planar images were simulated using the voxel-based digital phantoms created from each static planar validation acquisition setup. Image analysis was performed, as explained in Section 2.1.1 for the measured data.

As part of the simulation, SIMIND provides the percentage of penetrated photons after collimation. As this information was readily available, it was reported for the EPHDs.

### 2.2.2. Whole-body planar validation tests

SIMIND does not mimic any motion of the patient bed (Mcgurk 2007). Thus, to simulate a WB scan, the detector's length was defined as the scan length (i.e., the length of the patient bed), in this case, 200.0 cm. The WB simulation time was calculated according to Eq. (4), to ensure that the simulation mimics a measurement acquired at the specified patient bed scan speed.

$$WB \ simulation \ time \ (min) = \frac{length \ of \ physical \ detector \ (cm)}{scan \ speed \ (cm/min)} \qquad (4)$$

The WB simulation time equals 6.45 min, for a detector with length 38.7 cm and a scan speed of 6.0 cm/min. The voxel-based digital phantoms created for each planar validation test were used to simulate the WB planar images. The images were analysed as described in Section 2.1.2.

Considering that the WB planar simulation with SIMIND is a static process, the WB system spatial resolution was not repeated in a scatter medium, as it is assumed to be similar to static planar in-scatter spatial resolution.

### 2.2.3. SPECT validation test

The voxel-based digital phantom, of the sphere suspended in a water-filled cylindrical phantom was used to simulate SPECT data sets for the three isotope-collimator combinations. The SPECT projection images were reconstructed and analysed as for the measured data, described in Section 2.1.3.

### 2.3. Ethical approval

This study was performed with approval from the Health Sciences Research Ethics Committee at the University of the Free State, Ethics number UFS-HSD2019/2135/2502. The HSREC functions in compliance with, but not limited to, the following documents and guidelines: The SA

National Health Act. No. 61 of 2003; Ethics in Health Research: Principles, Structures and Processes (2015); SA GCP (2006); Declaration of Helsinki; The Belmont Report; The US Office of Human Research Protections 45 CFR 461 (for non-exempt research with human participants conducted or supported by the US Department of Health and Human Services- (HHS), 21 CFR 50, 21 CFR 56; CIOMS; ICH-GCP-E6 Sections 1, 2, 3, 4); The International Conference on Harmonization and Technical Requirements for Registration of Pharmaceuticals for Human Use (ICH Tripartite), Guidelines of the SA Medicines Control Council as well as Laws and Regulations with regard to the Control of Medicines, Constitution of the HSREC of the Faculty of Health Sciences at the University of the Free State.

## 3. Results

### 3.1. Static planar validation tests

#### 3.1.1. Energy pulse-height distributions

Figure 3 shows the measured and simulated extrinsic in-air EPHDs for all isotope-collimator combinations, at distances of 150 mm, 300 mm, and 650 mm, normalised to the respective main photopeaks of I-123 and I-131 (159.0 keV and 364.5 keV). It is important to note that the lower energy cut-off for the Siemens Symbia™ T16 gamma camera is at approximately 20.0 keV. Thus, photon energies below 20.0 keV are not reflected on any of the measured EPHDs.
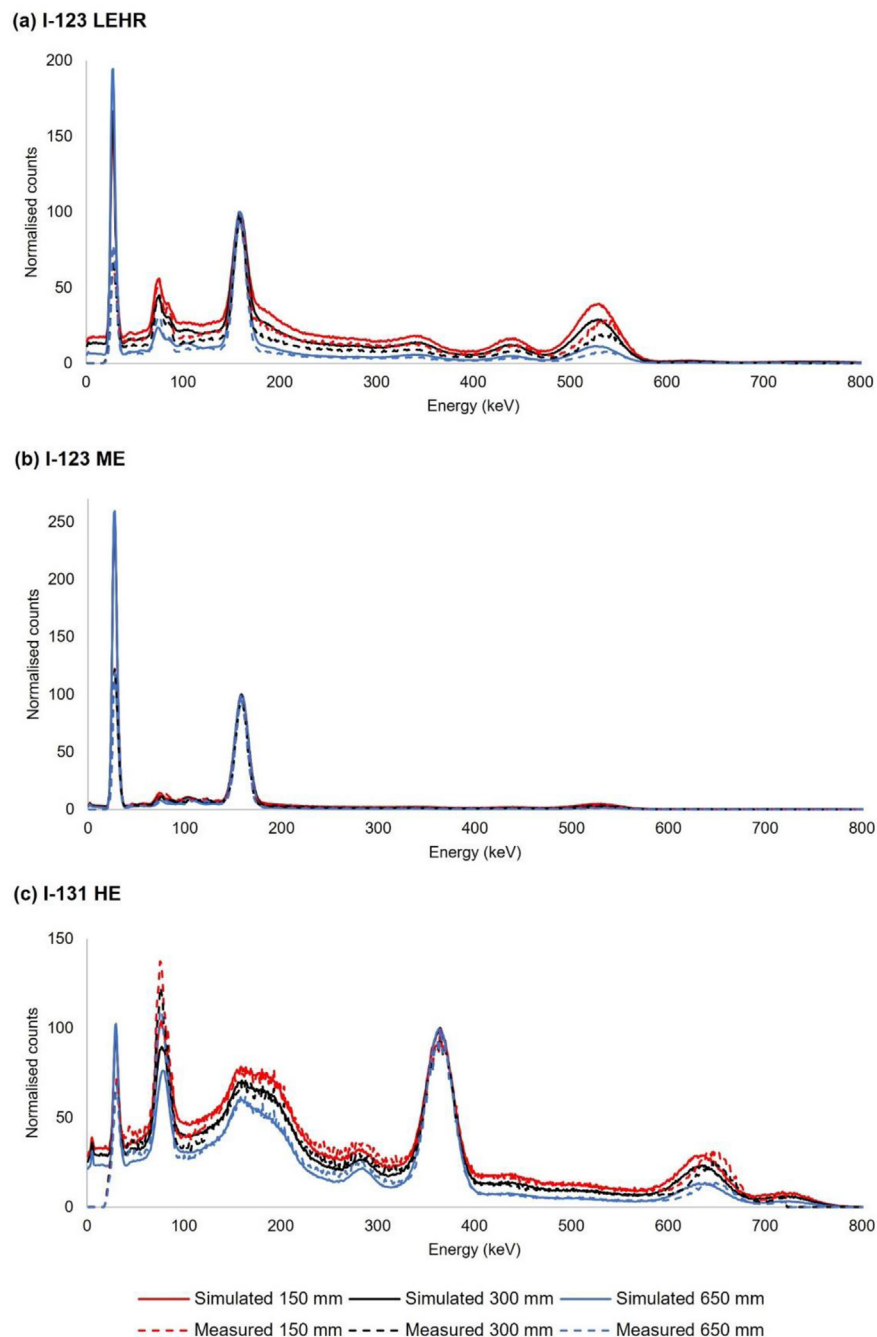


**Figure 3.** Comparison of the measured and simulated extrinsic EPHDs of a small point-like source at SCDs of 150 mm, 300 mm, and 650 mm, for (a) I-123 LEHR, (b) I-123 ME and (c) I-131 HE.

**Table 1.** Extrinsic in-air FWHM values and percentage simulated penetration photons for I-123 LEHR, I-123 ME, and I-131 HE, at SCDs of 150 mm, 300 mm, and 650 mm.

| Radionuclide, collimator and photopeak energy (keV) | Distance (mm) | FWHM (keV) | | Difference (keV) | *Simulated penetration photons (%) |
|---|---|---|---|---|---|
| | | Measured | Simulated | | |
| I-123 LEHR 159.0 | 150 | 18.1 ± 0.2 | 22.7 | 4.6 | 64.9 |
| | 300 | 16.7 ± 0.2 | 20.5 | 3.8 | 64.3 |
| | 650 | 15.4 ± 0.3 | 17.7 | 2.3 | 54.1 |
| I-123 ME 159.0 | 150 | 14.9 ± 0.3 | 16.9 | 2.0 | 23.2 |
| | 300 | 14.7 ± 0.3 | 16.8 | 2.1 | 21.6 |
| | 650 | 14.6 ± 0.3 | 16.6 | 2.0 | 13.7 |
| I-131 HE 364.5 | 150 | 39.0 ± 0.2 | 38.1 | -0.9 | 34.3 |
| | 300 | 36.9 ± 0.2 | 36.5 | -0.4 | 33.8 |
| | 650 | 34.7 ± 0.2 | 34.5 | -0.2 | 31.8 |

* Percentage simulated penetration photons after collimation.

**Table 2.** Static planar system sensitivity values for I-123 LEHR, I-123 ME and I-131 HE.

| | Sensitivity (cps/MBq) | | Difference (cps/MBq) | Percentage difference (%) |
|---|---|---|---|---|
| | Measured | Simulated | | |
| I-123 LEHR | 184.7 ± 0.09 | 172.0 | 12.7 | -6.9 |
| I-123 ME | 121.6 ± 0.07 | 123.4 | -1.8 | 1.5 |
| I-131 HE | 48.8 ± 0.02 | 48.8 | 0.0 | 0.0 |
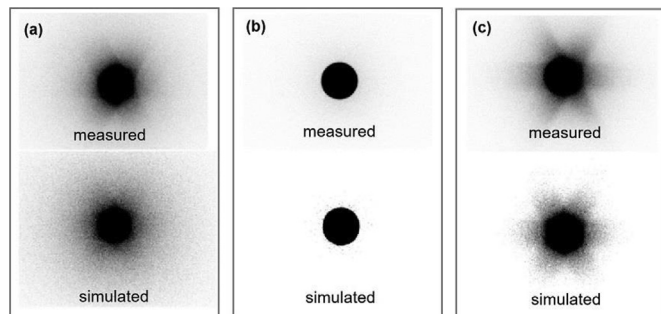


**Figure 4.** Measured and simulated static planar system sensitivity images, obtained from a petri-dish at a SCD of 100 mm, for (a) I-123 LEHR, (b) I-123 ME and (c) I-131 HE.

The FWHM values obtained from the main photopeaks for the I-123 and I-131 EPHDs shown in Figure 3 are reported in Table 1. The differences between the measured and simulated main photopeaks are also shown for the three isotope-collimator combinations. Average and standard deviation values are reported for the measurements. Standard deviations not exceeding 0.3 keV were reported. The largest discrepancy between the measured and simulated FWHM values and percentage simulated penetration photons was 4.6 keV and 64.9%, respectively, for I-123 LEHR at a SCD of 150 mm.

### 3.1.2. System sensitivity

Table 2 shows measured and simulated static planar system sensitivity values for the three isotope-collimator combinations. The system sensitivity values compare well for all isotope-collimator combinations. I-123 LEHR displayed the largest differences of 12.7 cps/MBq, which relates to 6.9% difference, between measured and simulated sensitivity values.

Figure 4 shows that the measured and simulated petri-dish images compare well for all isotope-collimator combinations. The starlike pattern, typical of collimator septal penetration with a hexagonal-shaped collimator hole, is evident on both the measured and simulated images of I-123 LEHR and I-131 HE.

### 3.1.3. In-air spatial resolution

The measured and simulated static planar system spatial resolution images and LSFs at a SCD of 100 mm, for the isotope-collimator combinations, are shown in Figure 5. The effects of septal penetration for I-123 LEHR and I-131 HE is visible in a raised tail region on the LSFs. Figure 6 shows the measured and simulated static planar system spatial resolution values (mm) in FWHM and FWTM, for all isotope-collimator combinations, at SCDs of 50, 100 and 150 mm. The error bars on the measured data represent two standard deviations. The measured and simulated FWHM and FWTM values compare well for all isotope-collimator combinations, with percentage differences not exceeding 6.4% and 10.0%, respectively.

### 3.1.4. In-scatter spatial resolution

The measured and simulated static planar system spatial resolution images and LSFs with 50 mm of scatter medium for the three isotope-collimator combinations, for a SCD of 100 mm, are shown in Figure 7. The corresponding resolution values (mm) are shown in Figure 8.

A good agreement is noted between the measured and simulated FWHM and FWTM values, with percentage differences not exceeding 5.8% and 12.6%, respectively. The LSFs shown in Figure 7 also confirm this.
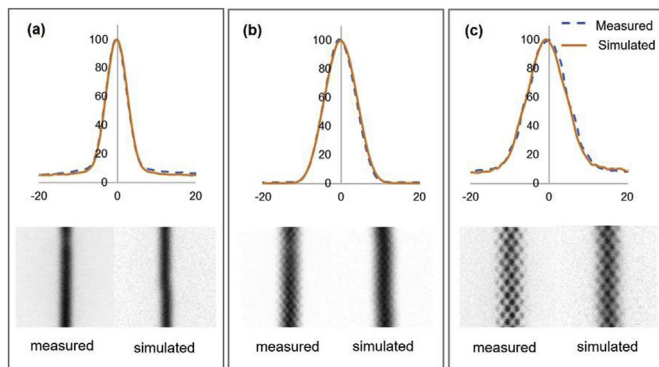
## 3.2. WB planar validation tests

### 3.2.1. System sensitivity

Table 3 shows measured and simulated WB planar system sensitivity values for the three isotope-collimator combinations. The measured and simulated WB planar system sensitivity values compare well. I-123 LEHR shows the largest deviation with a difference and percentage difference of 11.7 cps/MBq and 6.3%, respectively. The measured and simulated petri-dish images, shown in Figure 9, compare well.

### 3.2.2. In-air spatial resolution

Figure 10 shows the measured and simulated WB planar system spatial resolution images and LSFs, and Figure 11 the corresponding spatial resolution values (mm) in air for the three isotope-collimator

**Figure 5.** Measured and simulated LSFs and static planar system spatial resolution images of a capillary tube in air, at a SCD of 100 mm, for (a) I-123 LEHR, (b) I-123 ME and (c) I-131 HE.

combinations at a SCD of 100 mm. There are good agreements between the measured and simulated FWHM and FWTM values for all isotope-collimator combinations, and the percentage differences do not exceed 5.1% and 5.4%, respectively. The measured and simulated LSFs compare well for all isotope-collimator combinations.

### 3.3. SPECT validation tests

Measured and simulated SPECT sensitivity values for the three isotope-collimator combinations are shown in Table 4. The results show a good agreement for all isotope-collimator combinations, with differences and percentage differences not exceeding 2.5 cps/MBq and 3.6%, respectively. A transaxial slice through each of the reconstructed images is shown in Figure 12. Overall, the measured and simulated images compare well for all isotope-collimator combinations.

## 4. Discussion

Overall, the results show a good agreement between the measured and simulated validation results for planar (static and WB) and SPECT imaging.

### 4.1. Energy pulse-height distributions

The underestimation in the modelling of the ER for low photon energies with the fitted ER model, as described by Morphis et al. (2021), resulted in an increased amplitude of the 27.3 keV and the 29.6 keV photopeaks in the simulated EPHD of I-123 and I-131, respectively. This difference is further affected by the cut-off of photon energies below 20.0 keV. The small offset between the measured and simulated photopeaks, visible at the high-energy part of the I-123 and I-131 EPHD, is due to the nonlinear energy response of the physical gamma camera detector (Cherry et al., 2003). The small differences seen between the amplitudes of the measured and simulated high-energy photopeaks of I-123 and I-131 can be attributed to the normalisation of the EPHDs to their respective main emission photopeaks. Similar measurement-simulation comparisons have been reported in literature (Ejeh 2019; Tanaka et al., 2007); however, not necessarily using the SIMIND MC code.

Table 1 shows, as expected, a decrease in the percentage penetrated photons at increased SCD for all isotope-collimator combinations, which can also be seen in Figure 3. The effect of septal penetration is less pronounced for I-123 ME, as the percentage of photons penetrating the collimator is considerably less, thus, there is little difference between the EPHDs and the calculated FWHM values at the three distances. The minor difference between the measured and simulated EPHD for I-123 LEHR (indicated by the arrows on Figure 3a) can be attributed to the backscattering of high-energy photons from the second detector at large angles up to 180°. The contribution of scattering of the high-energy photons from the second detector was not included in the simulation. Figure 3b shows that the septal scatter and penetration components of I-123 ME are negligible, and because of this, we see a good comparison between the measured and simulated EPHD. However, for I-123 LEHR and I-131 HE, the high-energy photons will substantially contribute to the number of counts detected in the photopeak area due to Compton scattering in the collimator and penetration through the collimator septa. This emphasises the need for accurate collimator modelling in the compensation methods when aiming for an accurate activity quantification of the radioactivity in situations where these isotope-collimator combinations are used.
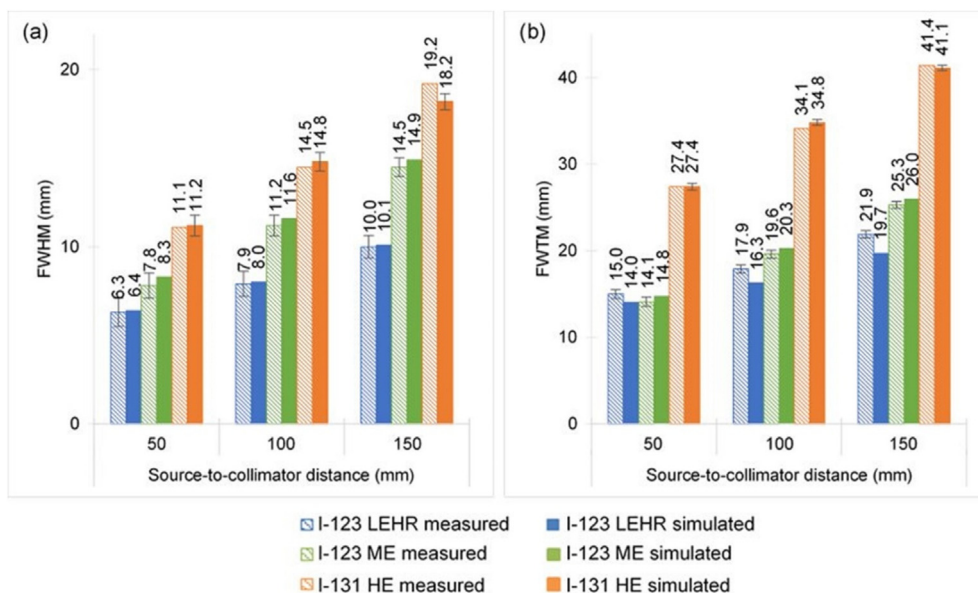


**Figure 6.** Measured and simulated static planar (a) FWHM and (b) FWTM values, obtained from capillary tubes in air, for SCDs of 50, 100 and 150 mm, for I-123 LEHR, I-123 ME and I-131 HE.
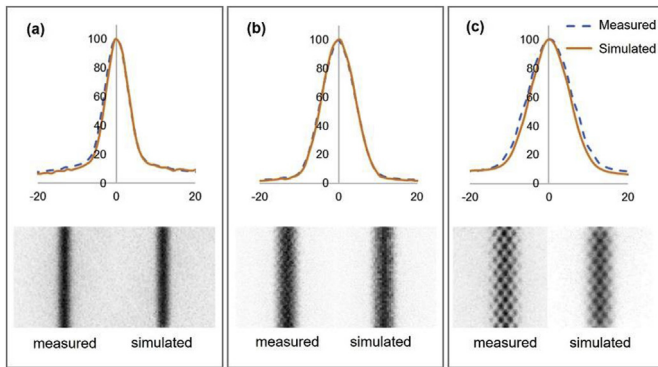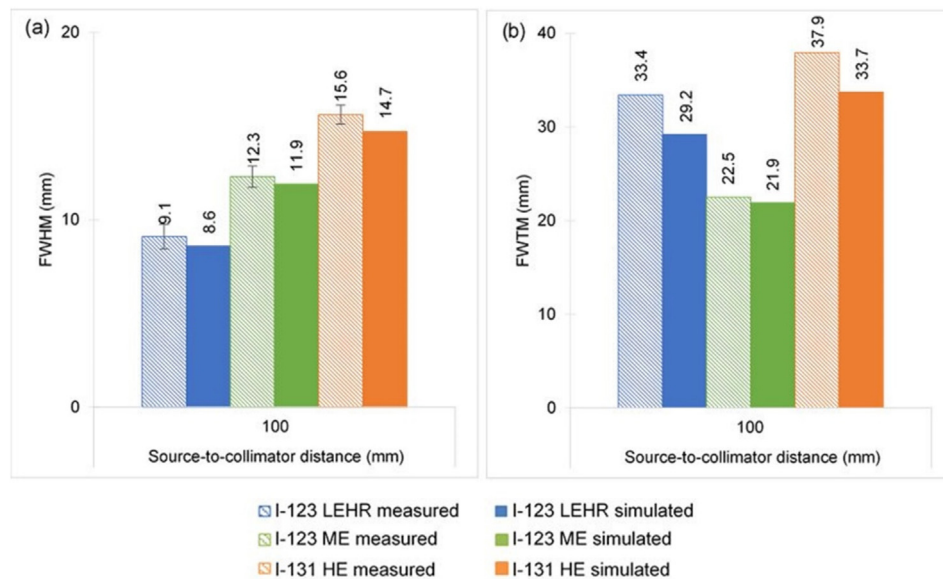
**Figure 7.** Measured and simulated LSFs and static planar system spatial resolution images with 50 mm of added scatter, at a SCD of 100 mm, for (a) I-123 LEHR, (b) I-123 ME and (c) I-131 HE.

### 4.2. System sensitivity

Accurate knowledge of the reference activity used to determine the system sensitivity value (static planar, WB planar and SPECT) is essential for quantitative imaging. The accuracy of the reference activity is dependent on the calibration of the dose calibrator for I-123 and I-131 which should be traceable to a secondary standards laboratory. During the calibration of the Biodex Atomlab 500 dose calibrator, performed by NMISA, it was found to underestimate the I-123 activity by 1.4% and overestimate the I-131 activity by 4.3%. From these results, correction factors were used when the I-123 and I-131 system sensitivity values were calculated.

The largest difference between the measured and simulated static planar and WB planar system sensitivity values were 6.9% (Table 2) and 6.3% (Table 3) for I-123 with the LEHR collimator, respectively. These discrepancies may also be attributed to scattered photons from the second detector, present in the measurement but not in the simulation. Discrepancies may also be attributed to small differences in source geometries used in this study and the geometries used by NMISA. NMISA also has an uncertainty in ascertaining the dose calibrator's accuracy. A good agreement was found between the simulated static and WB planar sensitivity values (Tables 2 and 3) for all three isotope-collimator combinations, with percentage differences not exceeding 1.2%. The measured and simulated static and WB planar images of the petri-dish source, as shown in Figures 4 and 9, respectively, compare well and the starlike patterns, typical of collimator septal penetration, are similar for the measured and simulated I-123 LEHR and I-131 HE images (Dewaraja et al., 2013; Ejeh et al., 2018; Westerberg, 2019). Similar results have been reported in literature for I-131 planar system sensitivity (Ejeh et al., 2018; Westerberg, 2019).

The SPECT sensitivity results corroborate with values reported in literature (Dewaraja et al., 2005; Ejeh 2019). The differences noted between the SPECT sensitivity values (Table 4) and the planar and WB system sensitivity values (Tables 2 and 3) are as expected and show the effect of collimator septal scatter and penetration. I-123 LEHR and I-131 HE have large amounts of collimator septal scatter and penetration, which is corrected for in the SPECT reconstruction process, but not for planar imaging. I-123 ME has significantly less collimator septal scatter and penetration, thus the difference between the planar and SPECT sensitivity values is much less. Both the measured and simulated reconstructed images (Figure 12) show the so-called Gibbs artefacts, when incorporating the collimator response compensation in the reconstruction process. These
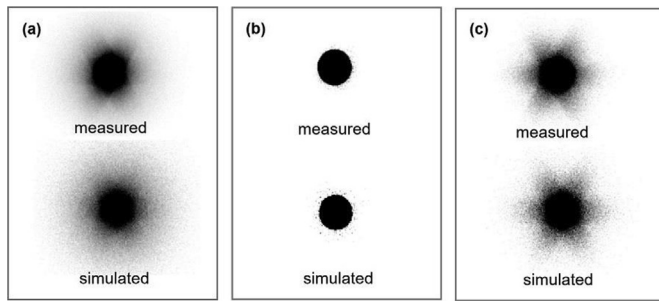


**Figure 8.** Measured and simulated static planar (a) FWHM and (b) FWTM values, with 50 mm of added scatter, for a SCD of 100 mm, for I-123 LEHR, I-123 ME and I-131 HE.

**Table 3.** WB planar system sensitivity values for I-123 LEHR, I-123 ME and I-131 HE.

| | Sensitivity (cps/MBq) | | Difference (cps/MBq) | Percentage difference (%) |
|---|---|---|---|---|
| | Measured | Simulated | | |
| I-123 LEHR | 184.9 ± 0.89 | 173.2 | 11.7 | -6.3 |
| I-123 ME | 120.4 ± 0.21 | 123.3 | 2.9 | 2.4 |
| I-131 HE | 48.3 ± 0.06 | 48.2 | 0.1 | -0.2 |

**Figure 9.** Measured and simulated WB planar system sensitivity images, obtained from a petri-dish at a SCD of 100 mm, for (a) I-123 LEHR, (b) I-123 ME and (c) I-131 HE.
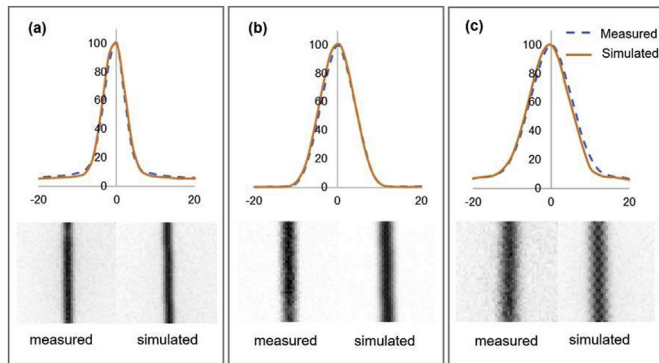


**Figure 10.** Measured and simulated LSFs and static WB system spatial resolution images of the capillary tubes in air, at a SCD of 100 mm, for (a) I-123 LEHR, (b) I-123 ME and (c) I-131 HE.

artefacts are characterised by increased count levels located at the edges of an object and a corresponding lower count level in the centre (Ljungberg et al., 2016). Small differences noted between measured and simulated SPECT sensitivity results may be attributed to the inconsistent VOI position across all scenarios, combined with the overestimated voxels at the sphere boundaries. Similar results have been reported in literature (Kangasmaa et al., 2011; Ramonaheng et al., 2020).

### 4.3. Spatial resolution

The measured and simulated FWHM values compare well for all isotope-collimator combinations, as shown in Figures 6 and 11, for static and WB planar system spatial resolution in air, respectively. As expected, the spatial resolution deteriorates with increasing SCD (Cherry et al., 2003). Both measured and simulated FWTM values for the static and WB planar images compare well for I-123 ME. Larger discrepancies are, however, noted for I-123 LEHR and I-131 HE, resulting in FWTM percentage differences of 10.0% and 5.4% for static and WB planar images, respectively.

Figure 5 reveals small discrepancies at the tail regions of I-123 LEHR LSF, which could explain the difference between the measured and simulated FWTM values, displayed in Figure 6. The measured and simulated LSFs for WB planar (Figure 10) compare well for all isotope-collimator combinations. However, minor discrepancies can be seen in the tail regions of the LSFs for I-123 LEHR and I-131 HE. This discrepancy correlates to the difference noted in the FWTM values reported in Figure 11.

The hexagonal pattern of holes, due to the construction of the collimator, can be seen on the static planar images obtained from I-123 ME and I-131 HE (Figure 5). Because of the necessity of large hole diameters and thicker septa, a lower spatial resolution can be expected (Autret et al., 2005; Ejeh et al., 2018). However, the pattern is less prominent on the WB planar measured I-123 ME and I-131 HE images (Figure 11). This may be attributed to the sources' movement relative to the detector during a WB planar acquisition – an effect that was not included in the static WB simulation.

When considering the system spatial resolution obtained from the in-air and in-scatter static planar images (Figures 6 and 8), the FWHM values compare well. The increased values of the measured FWTM, shown in Figure 8, originates from photons that were scattered in the scatter medium with a resulting photon energy that was absorbed in the NaI(Tl) crystal, and fell within the 15.0% imaging energy window due to the ER. Additionally, photons that originate from Compton scatterings in the collimator of the second detector, have a probability of being included in the measurement; however, this effect is not simulated and thus, may also contribute to discrepancies in the FWTM values. It is important to note that when describing the spatial resolution in terms of FWTM, the result will be affected by events from
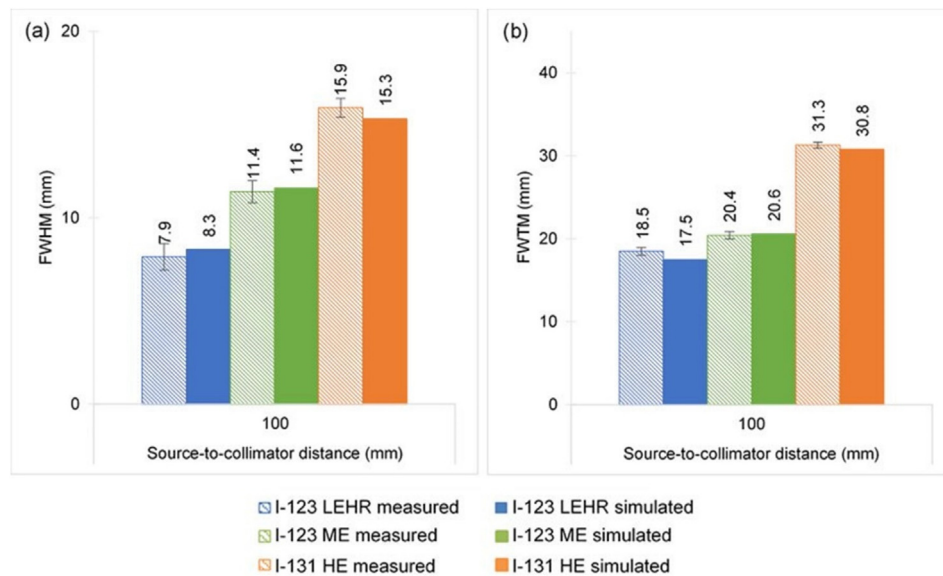


**Figure 11.** Measured and simulated WB planar (a) FWHM and (b) FWTM values obtained from the capillary tubes in air, at a SCD of 100 mm, for I-123 LEHR, I-123 ME, and I-131 HE.

**Table 4.** SPECT sensitivity values for I-123 LEHR, I-123 ME, and I-131 HE.

| | SPECT sensitivity (cps/MBq) | | Difference (cps/MBq) | Percentage difference (%) |
|---|---|---|---|---|
| | Measured | Simulated | | |
| I-123 LEHR | 84.2 ± 0.11 | 83.4 | 0.8 | -1.0 |
| I-123 ME | 121.4 ± 0.10 | 118.9 | 2.5 | -2.0 |
| I-131 HE | 22.4 ± 0.21 | 21.6 | 0.8 | -3.6 |
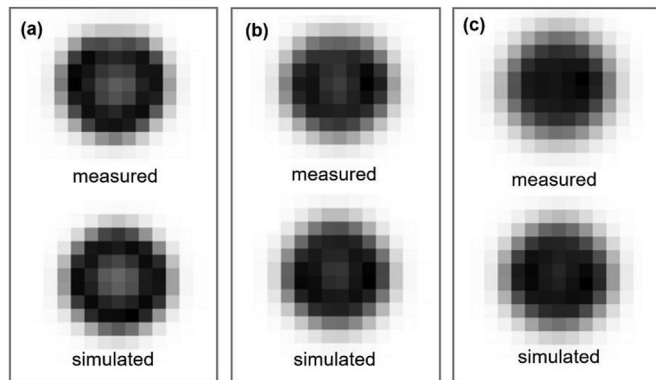


**Figure 12.** Transaxial slices through the reconstructed measured and simulated SPECT spheres in water for (a) I-123 LEHR, (b) I-123 ME and (c) I-131 HE.

potentially high-energy photon emissions, such as those that occur in the I-123 and I-131 decays. With the presence of septal scatter and penetration, the FWTM measurement can be problematic and is therefore often omitted (Autret et al., 2005). Similar to the in-air results, the small discrepancies between the measured and simulated FWTM values observed for I-123 LEHR and I-131 HE, are confirmed in the LSF tail regions, as shown in Figures 5 and 7.

Overall, the results show a better spatial resolution for I-123 LEHR than for I-123 ME. Thus, when imaging with I-123, the LEHR collimator would be better suited for studies prioritising spatial resolution. I-131 HE results in poorer spatial resolution in comparison to I-123. Similar results have been reported in literature (Autret et al., 2005; Dobbeleir et al., 1999; Ejeh et al., 2018; Rault et al., 2007).

## 5. Conclusion

Existing gamma camera models simulated with MC codes lack an accurate implementation of the gamma camera's energy response across all photon energies. Morphis et al. (2021) addressed this deficiency by implementing a fitted function which models the Siemens Symbia™ T16 gamma camera's energy response across all energies and used it together with the SIMIND MC code to improve the simulations with the gamma camera. In this study, we have validated this model by comparing results from physical measurements with the gamma camera to simulations with SIMIND using this improved fitted ER model for the isotope-collimator combinations: I-123 LEHR, I-123 ME, and I-131 HE.

Results show that when using I-123 and I-131 with the LEHR and HE collimator, respectively, appropriate collimator response corrections, including modelling of septal scatter and penetrations, are essential when accurate activity quantification is required. The use of a ME collimator for I-123 imaging reduces the effects of septal penetration and collimator scatter from the high-energy photons. The ME collimator is therefore a better choice when no septal scatter and penetration corrections are available.

Overall, this study has shown the SIMIND MC code's potential usefulness, combined with our improved ER model, to further develop activity quantification methods for I-123 and I-131 static planar, WB planar and SPECT acquisitions with the Siemens Symbia™ T16 gamma camera.

## Declarations

### Author contribution statement

Michaella Morphis, Johan A van Staden: Conceived and designed the experiments; Performed the experiments; Analyzed and interpreted the data; Contributed reagents, materials, analysis tools or data; Wrote the paper.

Hanlie du Raan, Michael Ljungberg: Conceived and designed the experiments; Analyzed and interpreted the data; Contributed reagents, materials, analysis tools or data; Wrote the paper.

### Data availability statement

Data included in article/supplementary material/referenced in article.

### Declaration of interests statement

The authors declare no conflict of interest.

### Additional information

No additional information is available for this paper.

## References

Autret, D., Bitar, A., Ferrer, F., Lisbona, A., Bardiès, M., 2005. Monte Carlo modeling of gamma cameras for I-131 imaging in targeted radiotherapy. Cancer Biother. Radiopharm. 20 (1), 77–84.

Bahreyni Toossi, M., Islamian, P.J., Momennezhad, M., Ljungberg, M., Naseri, S.H., 2010. SIMIND Monte Carlo simulation of a single photon emission CT. J. Med. Phys. 35 (1), 42.

Bombardieri, E., Giammarile, F., Aktolun, C., Baum, R.P., Bischof Delaloye, A., Maffioli, L., Moncayo, R., Mortelmans, L., Pepe, G., Reske, S.N., Castellani, M.R., Chiti, A., 2010. 131I/123I-Metaiodobenzylguanidine (MIBG) scintigraphy: procedure guidelines for tumour imaging. Eur. J. Nucl. Med. Mol. Imag. 37 (12), 2436–2446.

Cherry, S.R., Sorenson, J., Phelps, M.R., Methé, B.M., 2003. Physics in Nuclear Medicine, third ed. Saunders, Philadelphia.

Dewaraja, Y.K., Ljungberg, M., Green, A.J., Zanzonico, P.B., Frey, E.C., 2013. MIRD pamphlet No. 24: guidelines for quantitative 131I SPECT in dosimetry applications. J. Nucl. Med. 54 (12), 2182–2189.

Dewaraja, Y.K., Wilderman, S.J., Ljungberg, M., Koral, K.F., Zasadny, K., Kaminiski, M.S., 2005. Accurate dosimetry in 131I radionuclide therapy using patient-specific, 3-dimensional methods for SPECT reconstruction and absorbed dose calculation. J. Nucl. Med.: Off. Publ. Soc. Nuc. Med. 46 (5), 840–849. PMCID: PMC2804106.

Dobbeleir, A.A., Hambÿe, A.E., Franken, P.R., 1999. Influence of high-energy photons on the spectrum of iodine-123 with low- and medium-energy collimators: consequences for imaging with 123I-labelled compounds in clinical practice. Eur. J. Nucl. Med. 26 (6), 655–658.

Ejeh, J., 2019. Accuracy of Iodine-131 Activity Quantification and Dosimetry for Three-Dimensional Patient-specific Models. University of the Free State, South Africa [thesis].

Ejeh, J., van Staden, J.A., du Raan, H., 2018. Validation of SIMIND Monte Carlo simulation software form modelling a Siemens symbia T SPECT scintillation camera. IFMBE Proceedings 68 (1).

Ferreira, T., Rasband, W., 2012. ImageJ User Guide, p. 198 [online] Retrieved. http://imagej.nih.gov/ij/docs/guide/user-guide.pdf. (Accessed 10 February 2015).

Frey, E.C., Tsui, B.M.W., 1996. A New method for modeling the spatially-variant, object-dependent scatter response function in SPECT. In: 1996 IEEE Nucl. Sci. Symp. Conf. Rec. Vol. 2. IEEE, pp. 1082–1086.

Garkavij, M., Nickel, M., Sjogreen-Gleisner, K., Ljungberg, M., Ohlsson, T., Wingardh, K., Strand, S.E., Tennvall, J., 2010. Lu- [ DOTA0, Tyr3 ] octreotate therapy in patients with disseminated neuroendocrine tumors;: analysis of dosimetry with impact on future therapeutic strategy. Cancer 116 (4 Suppl), 1084–1092.

Giammarile, F., Chiti, A., Lassmann, M., Brans, B., Flux, G., 2008. "EANM procedure guidelines for 131I-Meta-Iodobenzylguanidine (131I-MIBG) therapy. Eur. J. Nucl. Med. Mol. Imag. 35 (5), 1039–1047.

Islamian, J.P., Taghi, M., Toossi, B., Momennezhad, M., Ljungberg, M., 2012. Simulation of a quality Control jaszczak phantom with SIMIND Monte Carlo and adding the phantom as an accessory to the program simulation of a quality Control jaszczak phantom with SIMIND Monte Carlo and adding the phantom as an accessory to the program. Iran. J. Med. Phys. 9 (2), 135–140.

Jan, S., Benoit, D., Becheva, E., Carlier, T., Cassol, F., Descourt, P., Frisson, T., Grevillot, L., Guigues, L., Maigne, L., Morel, C., Perrot, Y., Rehfeld, N., Sarrut, D., Schaart, D.R., Stute, S., Pietrzyk, U., Visvikis, D., Buvat, I., Zahra, N., 2011. GATE V6;: a major enhancement of the GATE simulation platform enabling modelling of CT and radiotherapy. Phys. Med. Biol. 56 (4), 881–901.

Kalantari, F., Rajabi, H., Saghari, M., 2012. Quantification and reduction of the collimator-detector response effect in SPECT by applying a system model during iterative image reconstruction: a simulation study. Nucl. Med. Commun. 33 (3), 228–238.

Kangasmaa, T., Sohlberg, A., Kuikka, J.T., 2011. Reduction of collimator correction artefacts with bayesian reconstruction in spect. Int. J. Mol. Imaging 2011, 6.

Kellett, M.A., Arinc, A., Bé, M.M., Browne, E., Chechev, V.P., Chisté, V., Dersch, R., Helmer, R.G., Huang, X., Kibedi, T., Kondev, F.G., Kuzmenko, N.K., Luca, A., MacMahon, T.D., Mougeot, X., Nichols, A., Pearce, A., Schonfeld, E., Vavin, V., Castro, R.M., Wang, B., Wu, S., 2017. Laboratoire National Henri Becquerel [online]. Retrieved. http://www.lnhb.fr/en/. (Accessed 17 June 2020).

Ljungberg, M., Strand, S.E., 1989. A Monte Carlo program for the simulation of scintillation camera characteristics. Comp. Meth. Prog. Bio. 29 (4), 257–272.

Ljungberg, M., Strand, S.E., King, M.A., 1998. Monte Carlo Calculations in Nuclear Medicine: Applications in Diagnostic Imaging. CRC Press.

Ljungberg, M., Celler, A., Konijnenberg, M.W., Eckerman, K.F., Dewaraja, Y.K., Sjögreen-Gleisner, K., 2016. MIRD pamphlet No. 26: joint EANM/MIRD guidelines for quantitative 177Lu SPECT applied for dosimetry of radiopharmaceutical therapy. J. Nucl. Med. 57 (1), 151–162.

Ljungberg, M., Gleisner, K., 2015. Hybrid imaging for patient-specific dosimetry in radionuclide therapy. Diagnostics 5 (3), 296–317.

Ljungberg, M., Strand, S.E., King, M.A., 2012. Monte Carlo Calculations in Nuclear Medicine: Second Edition - Applications in Diagnostic Imaging. 2nd Ed.

Loening, A.M., Gambhir, S.S., 2001. AMIDE: a completely free system for medical imaging data analysis. J. Nucl. Med. 42 (5), 192.

Mcgurk, R.J., 2007. Variation of Image Counts with Patient Anatomy and Development of a Monte Carlo Simulation System for Whole-Body Bone Scans. University of Canterbury, New Zealand [thesis].

Minarik, D., Sjögreen Gleisner, K., Ljungberg, M., 2008. Evaluation of quantitative 90Y SPECT based on experimental phantom studies. Phys. Med. Biol. 53, 5689–5703.

Morphis, M., van Staden, J.A., du Raan, H., Ljungberg, M., 2021. Modelling of energy-dependent spectral resolution for SPECT Monte Carlo simulations using SIMIND. Heliyon 7 (12), e06097.

National Electrical Manufacturers Association, 2012. NEMA Standards Publication NU 1–2012: Performance Measurements of Gamma Cameras, p. 50.

Ramonaheng, K., van Staden, J.A., du Raan, H.R., 2020. Validation of a Monte Carlo modelled gamma camera for lutetium-177 imaging. Appl. Radiat. Isot. 163, 109200.

Rault, E., Vandenberghe, S., Van Holen, R., De Beenhouwer, J., Staelens, S., Lemahieu, I., 2007. Comparison of image quality of different iodine isotopes (I-123, I-124, and I-131). Cancer Biother. Radiopharm. 22 (3), 323.

Sarrut, D., Bardiès, M., Boussion, N., Freud, N., Jan, S., Létang, J., Maigne, L., Marcatili, S., Mauxion, T., Papadimitroulas, P., Perrot, Y., Pietrzyk, U., Robert, C., Schaart, D.R., Visvikis, D., Buvat, I., 2014. A review of the use and potential of the GATE Monte Carlo simulation code for radiation therapy and dosimetry applications A review of the use and potential of the GATE Monte Carlo simulation code for radiation therapy and dosimetry applications. Med. Phys. 41 (6), 64301, 1–14.

Silberstein, E.B., 2012. Radioiodine: the classic theranostic agent. Semin. Nucl. Med. 42 (3), 164–170.

Sjögreen, K., Ljungberg, M., Strand, S.E., 2002. An activity quantification method based on registration of CT and whole-body scintillation camera images, with application to I131. J. Nucl. Med. 43 (7), 972–982. PMID: 12097471.

Sjögreen, K., Ljungberg, M., Wingårdh, K., Minarik, D., Strand, S.E., 2005. The LundADose method for planar image activity quantification and absorbed-dose assessment in radionuclide therapy. Cancer Biother. Radiopharm. 20 (1), 92–97.

Staelens, S., Strul, D., Santin, G., Vandenberghe, S., Koole, M., Asseler, Y.D., 2003. Monte Carlo simulations of a scintillation camera using GATE: validation and application modelling. Phys. Med. Biol. 48 (18), 3021–3042.

Tanaka, M., Uehara, S., Kojima, A., 2007. Monte Carlo simulation of energy spectra for 123I. Phys. Med. Biol. 52, 4409–4425.

Thomas, S.R., 2002. Options for radionuclide therapy: from fixed activity to patient-specific treatment planning. Cancer Biother. Radiopharm. 17 (1084-9785 SB-IM), 71–82.

Westerberg, F., 2019. Quantification of I-131 Activity from Gamma Camera Images of Thyroid Cancer Patients. Lund University, Sweden [thesis].

Yordanova, A., Eppard, E., Kürpig, S., Bundschuh, R.A., Schönberger, S., Gonzalez-carmona, M., Feldmann, G., 2017. Theranostics in nuclear medicine practice. OncoTargets Ther. 10, 4821–4828.

Zaidi, H., 1999. Relevance of accurate Monte Carlo modeling in nuclear medical imaging. Med. Phys. 26 (February), 574–608.